Shear banding in a lyotropic lamellar phase. I. Time-averaged velocity profiles

Jean-Baptiste Salmon, Sébastien Manneville,* and Annie Colin

Centre de Recherche Paul Pascal, Avenue Schweitzer, 33600 Pessac, France

Using velocity profile measurements based on dynamic light scattering and coupled to structural and rheological measurements in a Couette cell, we present evidences for a shear banding scenario in the shear flow of the *onion* texture of a lyotropic lamellar phase. *Time-averaged* measurements clearly show the presence of structural shear banding in the vicinity of a shear-induced transition, associated with the nucleation and growth of a highly sheared band in the flow. Our experiments also reveal the presence of slip at the walls of the Couette cell. Using a simple mechanical approach, we demonstrate that our data confirm the classical assumption of the shear banding picture, in which the interface between bands lies at a given stress $\sigma*$. We also outline the presence of large temporal fluctuations of the flow field, which are the subject of the second part of this paper [Salmon *et al.*, Phys. Rev. E **68**, 051504 (2003)].

PACS number(s): 83.10.Tv, 47.50.+d, 83.85.Ei

I. INTRODUCTION

A wide class of materials, referred to as *complex fluids*, exhibit a common feature: when submitted to a shear stress σ, their flow cannot be described easily as in the case of simple fluids [1]. Indeed, the flow of simple liquids is entirely determined by the knowledge of the viscosity η: when submitted to a shear stress σ far from any hydrodynamic instability and after a very short transient, the velocity profile is linear and characterized by a shear rate $\dot{\gamma}$, given by the linear relation $\dot{\gamma} = \sigma/\eta$ [2]. In the case of complex fluids, such a linear relation between σ and $\dot{\gamma}$ does not hold any more. In polymeric fluids, for instance, the flow tends to decrease the *effective viscosity* $\eta \hat{=} \sigma/\dot{\gamma}$, whereas disordered media such as emulsions or foams can resist elastically to a small applied stress but flow plastically under large σ [1]. Such behaviors are due to the presence of a supramolecular architecture that leads to a coupling between the structure of the fluid and the flow [3]. The *shear-thinning* effect in polymeric fluids, for instance, is due to the alignment of the polymer chains along the flow direction, whereas the crossover between *pasty* and fluid states in glassy materials is attributed to microscopic rearrangements of the structure [4].

In some cases, because of a strong flow-structure coupling, the flow can *induce* new organizations. In wormlike micellar systems, for instance, a shear flow can induce a nematic phase [5,6]. In lamellar phases, shear may induce structures that do no exist at rest, e.g., the *onion* texture [7,8]. Such *shear-induced structures* (SIS) have been observed in a lot of complex fluids, especially in lyotropic systems [9–11]. These behaviors are generally associated with a *spatial structuration* of the fluid: the SIS nucleates at a critical stress or a critical shear rate and expands in the flow as σ (or $\dot{\gamma}$) is increased. Since the viscosity of the SIS differs from that of the original structure, the flow field is assumed to be composed of two macroscopic *bands* of different shear rates. This behavior, generically called *shear banding*, seems to be a universal feature of complex fluids. Its microscopic origin is not yet clearly understood: the shear banding behavior may arise from elastic instabilities [12], from frozen disorder and local plastic events [13] or from a coupling between shear flow and a phase transition [14]. Numerous phenomenological descriptions of shear banding have emerged during the last decade (see Refs. [15–19], and references therein). Those theoretical approaches have undoubtedly helped to understand the experiments, while not always providing a microscopic description of the phenomenon.

Most of experimental works rely on rheological data and structural measurements. In those experiments, shear banding is attributed to the presence of a *stress plateau* on the flow curve associated with a structural change, observed, for instance, using x-ray diffraction techniques [5,6,10] or direct visualizations of birefringence bands in the flow field [20,21]. Recently, a few experiments using nuclear magnetic resonance velocimetry have evidenced the fact that velocity profiles in such systems may display bands of different shear rates [22,23]. However, some of these experiments have reported a contradictory picture for the shear banding instability: it seems that the observed structural bands do not always correspond to bands of different shear rates, at least in a specific wormlike micellar system [24]. More recently, experiments based on dynamic light scattering velocimetry performed in our group have revealed a classical shear banding phenomenology in another wormlike micellar system [25]. Therefore, more experimental data are needed to fully understand the spatial structuration of the flow field in the general SIS and shear-banding phenomenon.

The aim of this paper is to perform an extensive study of shear banding in a specific complex fluid, a *lyotropic lamellar* phase. This system is known to exhibit a shear-induced transition, called the *layering* transition, between two different *textures* of the phase [26,27]. In the present paper, we present *time-averaged* velocimetry measurements performed simultaneously to structural measurements using, respectively, dynamic and static light scattering techniques.

This paper is organized as follows. In Sec. II, we briefly describe the system under study and the experimental setup allowing us to measure both the structure of the fluid and its

---

*Electronic address: sebm@crpp-bordeaux.cnrs.fr

rheological behavior. In Sec. III, we present the experimental setup for measuring velocity profiles in a Couette flow [28]. Section IV describes the experiments performed at a given temperature ($T=30$ °C) and under controlled shear rate. These experiments support the classical picture of shear banding in this particular system and our data also reveal the presence of wall slip, which is consistent with the observed shear banding scenario. A detailed mechanical analysis based on wall slip measurements and rheological data is presented in Sec. V and helps us demonstrate that the classical mechanical assumption of shear banding, in which the interface between the bands is only stable at a given stress, holds in our experiments. We then briefly summarize our results in Sec. VI, and emphasize on the puzzling presence of temporal fluctuations of the flow field near the shear-induced transition. The study of these temporal fluctuations are presented in a related paper where the link with *rheochaos* is emphasized [29].

II. GLOBAL RHEOLOGY OF THE ONION TEXTURE NEAR THE LAYERING TRANSITION

A. Rheology of lyotropic lamellar phases: The *onion* texture

Lyotropic systems are composed of surfactant molecules in a solvent. Because of the chemical duality of the surfactant molecules (polar head and long hydrophobic chain), self-assembled structures at the nanometer scale are commonly observed [1]. Depending on the range of concentrations, one can observe different structures: for instance, long cylinders of some microns long (*wormlike micelles*) or infinite surfactant bilayers (*membranes*). In the latter case, because of the interactions, the membranes can form periodic stacks, referred to as *lamellar* phases and noted L_α, or randomly connected continuous structures, called *sponge* phases and noted L_3 [30,31]. In a lamellar phase, the smectic period d, i.e., the distance between the bilayers, ranges from a few nanometers up to 1 μm whereas the thickness δ of the membranes is 2–4 nm. These liquid crystalline phase are locally organized as a monocrystal of smectic phase. If no specific treatment is applied, lyotropic lamellar phases contain at larger length scales (≈ 10 μm) a lot of characteristic defects: the organization of these defects is called the *texture* of the phase.

Since the work of Roux and co-workers, great experimental effort has been devoted to the understanding of the effect of a shear flow on lamellar phases [7,8]. A robust experimental fact has emerged: the shear flow controls the texture of the phase. For most systems, the experimental behavior usually observed is as follows.

(i) At very low shear rates ($\dot{\gamma} \lesssim 1$ s^{-1}), the membranes tend to align with the direction of the flow but textural defects still persist.

(ii) Above a critical shear rate of about $\dot{\gamma} \approx 1$ s^{-1}, the membranes are wrapped into monodisperse multilamellar vesicles called *onions* and organized as a disordered close-compact texture. The characteristic size R of this shear-induced structure (the onion size) is of the order of a few microns.
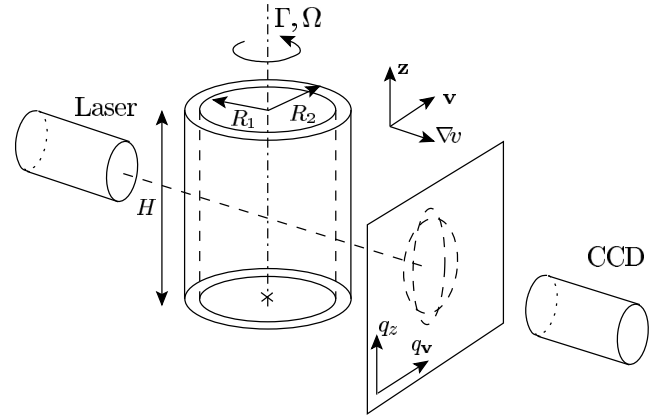

FIG. 1. Experimental setup. A thermostated plate (not shown) on top of the cell allows us to avoid evaporation. The rheometer imposes a constant torque Γ on the axis of the Couette cell and records its rotation speed Ω. The geometry of the Couette cell is $H = 30$ mm, $R_1 = 24$ mm, and $R_2 = 25$ mm, leading to a gap width $e = R_2 - R_1 = 1$ mm.

(iii) At higher shear rates ($\approx 10^3$ s^{-1}), perfectly ordered lamellar phases are recovered [7]. For some specific systems and at intermediate shear rates, spatial organizations of onions are sometimes encountered [26,27].

The complex fluid investigated here corresponds to this last behavior. It is made of sodium dodecyl sulfate (SDS) and octanol (surfactant molecules) in brine (solvent). At the concentrations considered here (6.5 wt % SDS, 7.8 wt %. Octanol, and 85.7 wt % Brine at 20 g L^{-1}), a lamellar phase is observed [32]. The smectic period d is 15 nm and the bilayers thickness δ is about 2 nm. For the given range of concentrations, the lamellar phase is stabilized by undulating interactions [33]. This system is very sensitive to temperature: for $T \gtrsim T_{L_\alpha\text{-}L_3} \approx 35$ °C, a sponge-lamellar phase mixture appears.

To study the effect of shear flow on this phase, we used the experimental device sketched in Fig. 1. A rheometer (TA Instruments AR1000N) and a Couette cell made of Plexiglas (gap $e=1$ mm, inner radius $R_1=24$ mm, and height $H = 30$ mm) allows us to perform rheological measurements. The rheometer imposes a constant torque Γ on the axis of the Couette cell which induces a constant stress σ in the fluid. The rotation speed Ω of the Couette cell is continuously recorded, from which the shear rate $\dot{\gamma}$ can be deduced. A computer-controlled feedback loop on the applied torque Γ can also be used to apply a constant shear rate without any significant temporal fluctuations ($\delta\dot{\gamma}/\dot{\gamma} \approx 0.01\%$).

Let us note σ and $\dot{\gamma}$ the shear stress and the shear rate indicated by the rheometer. The relations between ($\sigma, \dot{\gamma}$) and (Γ, Ω) read

$$\sigma = \frac{R_1^2 + R_2^2}{4\pi H R_1^2 R_2^2} \Gamma, \quad (1)$$

$$\dot{\gamma} = \frac{R_1^2 + R_2^2}{R_2^2 - R_1^2} \Omega. \quad (2)$$

Such definitions ensure that $(\sigma, \dot{\gamma})$ correspond to the average values of the local stress $\sigma(r)$ and shear rate $\dot{\gamma}(r)$ in the case of a Newtonian fluid (r denotes the radial position in the gap of the Couette cell). It is very important not to confuse the *averaged* quantities $(\sigma, \dot{\gamma})$, also referred to as the *engineering* quantities, with the local quantities $(\sigma(r), \dot{\gamma}(r))$. Moreover, it is also crucial to keep in mind that the shear rate $\dot{\gamma}$ given by the rheometer may differ from the *true* shear rate in the sample when wall-slip or inhomogeneous flows are present. In the following, the nature (engineering, *local* or *true*) of the variables will be specified whenever confusion is possible.

Temperature is controlled within $\pm 0.1\,°\mathrm{C}$ using a water circulation around the cell. A polarized laser beam (He-Ne, $\lambda = 632.8$ nm) is directed through the transparent Couette cell to investigate the effect of a shear flow on the structure of the fluid. Since the characteristic sizes of the texture are about 1 μm, well-defined diffraction patterns are obtained and recorded on a charge-coupled device camera (CCD, Cohu). As shown in Fig. 1, the laser beam crosses the sample twice, so that two diffraction patterns are recorded; the first one has an elliptical shape due to the optical refractions induced by the Couette geometry.

B. The layering transition: Stationary state and rheological chaos

Figure 2(a) shows a typical flow curve obtained on our lamellar phase at imposed stress or imposed shear rate for $T < T_c \approx 27\,°\mathrm{C}$. After a transient phase (at least 10–30 min), a stationary state is obtained, i.e., σ ($\dot{\gamma}$) does not vary significantly in time when $\dot{\gamma}$ (σ, respectively) is imposed. At low stress, the diffraction patterns are uniform rings indicating the presence of a disordered texture of onions. When σ reaches σ_c (≈ 15 Pa), six peaks appear on the ring indicating that the onions get a long range hexagonal order on layers sliding onto each other (see Fig. 2) [26,27]. Those layers lie in the $(\mathbf{v}, \mathbf{z})$ plane normally to the shear gradient direction ∇v. When σ is increased further, peaks become more contrasted. Note that the peaks with wave vectors along the rheometer axis $\mathbf{q}_z$ are less intense than the others. This is due to the zigzag motion of the planes of onions when sliding onto each other [27]. This shear-induced ordering transition, called the layering transition, has been observed in many monodisperse colloidal systems since the pioneering work of Ackerson and Pusey [34]. This ordering transition is associated with a shear thinning of the fluid, i.e., the ordering of the colloids causes the decrease of the viscosity.

More recently, complex dynamical behaviors have been observed in the vicinity of the layering transition for temperatures $T > T_c \approx 27\,°\mathrm{C}$ (see Fig. 2) and under controlled stress: the shear rate does not reach a stationary value, but sometimes oscillates indefinitely in time [35,36]. However, when the shear rate is imposed, no oscillations are observed and the responses of the shear stress seem almost stationary. In the stress imposed case, the shear rate oscillations are characterized by a large period of about 10 min. Moreover, the dynamics of the shear rate is correlated to a dynamical
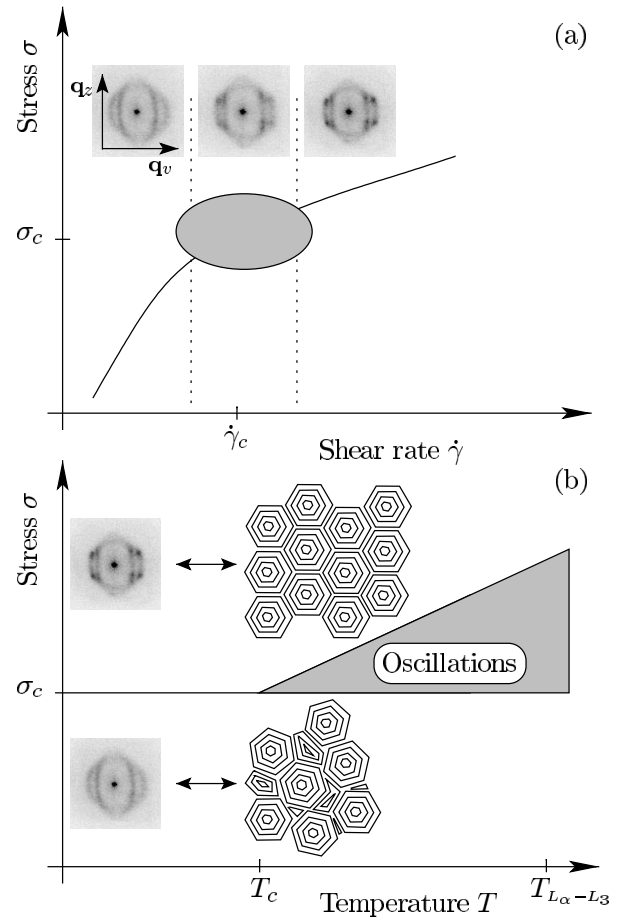

FIG. 2. (a) Typical flow curve of the onion texture. The diffraction pattern corresponds to the structure under shear. The gray area indicates the region of the oscillations of the shear rate at imposed stress for $T \gtrsim T_c \approx 27\,°\mathrm{C}$. (b) Shear diagram σ vs T. Oscillations of the shear rate at imposed stress appear for temperature $T \gtrsim T_c \approx 27\,°\mathrm{C}$. Shown are the schematic representations of the disordered and ordered states. $T_{L_\alpha\text{-}L_3} \approx 35\,°\mathrm{C}$ in the system under study.

structural change: the fluid oscillates between the disordered and the layered states. The origin of such surprising dynamics is not yet understood, but it is now quite clear that it does not correspond to a simple hydrodynamic or elastic instability. Even more complex dynamics, such as aperiodic oscillations or irregular fluctuations were measured, which were recently coined rheochaos [37,38]. In a previous work [36], a detailed study of such dynamics was performed: depending on the applied stress, several dynamical regimes have been found. Using dynamical system theory, a careful analysis has revealed that the dynamics do not simply correspond to a low-dimensional chaotic system, probably because some spatial degrees of freedom are involved. Moreover, rheological experiments performed with different gap widths e support the assumption of a spatial organization of the flow in the gap [36]. Our idea was that spatial structures such as *bands*, which lie in the ∇v direction and oscillate in time, could lead to the observed dynamics. Therefore, it was essential to measure the *local* velocity rather than the rotation speed Ω of the Couette cell.
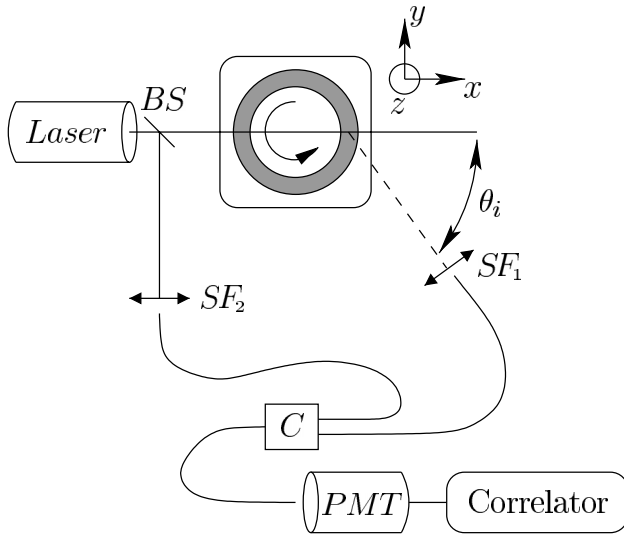
FIG. 3. Heterodyne DLS setup. BS denotes a beam splitter, SF spatial filters, and C the device coupling optical fibers and used to perform the interference between the scattered light and the reference beam.

In the following section, we present the experimental setup allowing us to perform velocimetry measurements. We then focus on experiments performed on *rheological stationary states* at $T = 30\,°C$ and under controlled shear rate.

III. EXPERIMENTAL SETUP: LOCAL VELOCIMETRY USING DYNAMIC LIGHT SCATTERING (DLS)

In order to evidence the possibility of a spatial organization of the fluid flow near the layering transition, we have used the experimental setup sketched in Fig. 3 and described in more detail in Ref. [28]. It consists of a classical heterodyne dynamic light scattering experiment mounted around a rheometer. Local velocity measurements using heterodyne DLS rely on the detection of the Doppler frequency shift associated with the motion of the scatterers inside a small scattering volume $\mathcal{V}$ [39–43]. In classical heterodyne setups, light scattered by the sample under study is collected along a direction θ_i and is made to interfere with a reference beam. Light resulting from the interference is sent to a photomultiplier tube and the autocorrelation function $C(\tau)$ of the intensity is computed using an electronic correlator.

When the scattering volume $\mathcal{V}$ is submitted to a shear flow, it can be shown that the correlation function $C(\tau)$ is an oscillating function of the time lag τ modulated by a slowly decreasing envelope. The frequency of the oscillations in $C(\tau)$ is exactly the Doppler shift $\mathbf{q} \cdot \mathbf{v}$, where $\mathbf{q}$ is the scattering wave vector and $\mathbf{v}$ is the local velocity averaged over the size of the scattering volume $\mathcal{V}$. In the experiments presented here, the imposed angle $\theta_i = 62.5°$ has been chosen in such a way that the size of $\mathcal{V}$ is about 50 μm [28]. Figure 4(a) shows a typical correlation function measured on a sheared latex suspension. The frequency shift $\mathbf{q} \cdot \mathbf{v}$ is recovered by interpolating a portion of $C(\tau)$ and looking for the zero crossings. Error bars on such measurements are ob-
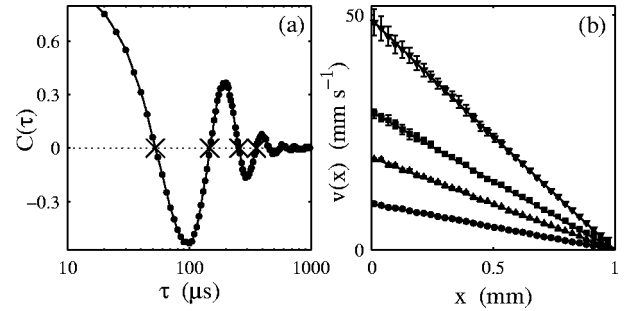

FIG. 4. (a) Experimental heterodyne correlation function (●) recorded on a latex suspension at $\dot{\gamma} = 10$ s^{-1}. The solid line corresponds to an interpolation of the heterodyne function from which the frequency shift $\mathbf{q} \cdot \mathbf{v}$ is computed. (b) Different velocity profiles obtained for various applied shear rates, $\dot{\gamma} = 10$ (●), 20 (▲), 30 (■), and 50 s^{-1} (▼). The solid lines are the expected velocity profiles for a Newtonian fluid.

tained through the fitting procedure: typical uncertainties are less than 5%.

The rheometer sits on a mechanical table whose displacements are controlled by a computer. Three mechanical actuators allow us to move the rheometer in the x, y, and z directions with a precision of 1 μm. Once y is set so that the incident beam is normal to the cell surface, velocity profiles are measured by moving the mechanical table in the x direction by steps of 30 μm.

As discussed in Ref. [28], going from $\mathbf{q} \cdot \mathbf{v}$ as a function of the table position to the velocity profile $v(x)$ requires a careful calibration procedure to take into account the refraction effects due to the Couette cell. x denotes the position of the scattering volume inside the gap. $x = 0$ ($x = e$) corresponds to the rotor (stator). Figure 4(b) presents velocity profiles measured at various known shear rates during the calibration using a Newtonian suspension of latex spheres in a water-glycerol mixture. This simple liquid has the same optical index ($n = 1.35$) as the lamellar phase under study. Finally, we accumulate the correlation functions over 3–5 s so that a full velocity profile with a resolution of 30 μm takes about 3 min to complete.

IV. LOCAL RHEOLOGY OF THE ONION TEXTURE NEAR THE LAYERING TRANSITION

A. Global rheology and local velocimetry

To understand the coupling between spatial degrees of freedom, global rheology, and the structural transition, we first present measurements obtained at $T = 30\,°C$ in the shear rate imposed mode. Well-defined rheological stationary states are obtained with such a method (see Sec. II B). We record engineering (i.e., global) rheological data simultaneously to the velocity profile measurements. In order to obtain reproducible experiments, careful rheological protocols must be used as discussed in Ref. [36]. At the temperature under study ($T = 30\,°C$), we apply a first step at $\dot{\gamma} = 5$ s^{-1} during 7200 s. This step of applied shear rate allows us to begin the experiment with a well-defined stationary
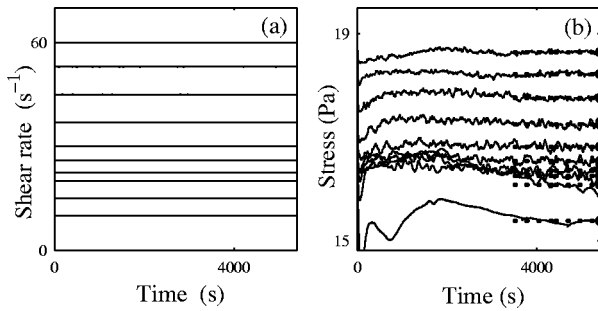
FIG. 5. $T = 30\,°C$. (a) Applied steps of shear rate. No significant temporal fluctuations are observed. (b) Corresponding temporal responses of $\sigma(t)$. The dotted lines indicate the part of the time series where the average stress ($\bullet$) is computed.

state of disordered onions. We then apply increasing shear rates for 5400 s per step. The increment between two steps is $\delta\dot{\gamma} = 2.5 - 5$ s^{-1}. The smaller value of $\delta\dot{\gamma}$ is chosen when a fine resolution is needed in the vicinity of the transition. As shown in Fig. 5(b), the temporal responses of the shear stress are almost stationary: small temporal fluctuations ($\delta\sigma/\sigma \approx 1\% - 3\%$) can be detected. Note that in the shear rate imposed mode the temporal fluctuations of $\dot{\gamma}$ are completely negligible ($\delta\dot{\gamma}/\dot{\gamma} \approx 0.01\%$ [see Fig. 5(a)]).

Engineering rheological measurements are displayed in Fig. 6 and the corresponding diffraction patterns at various applied shear rates are shown in Figs. 6(a–f). For shear rates below $\dot{\gamma}_c \approx 15$ s^{-1}, diffraction patterns are uniform rings indicating that the structure of the onions is disordered [Figs. 6(a,b)]. Above $\dot{\gamma}_c$, six fuzzy peaks appear on the diffraction ring, indicating the onset of the layering transition [Fig.
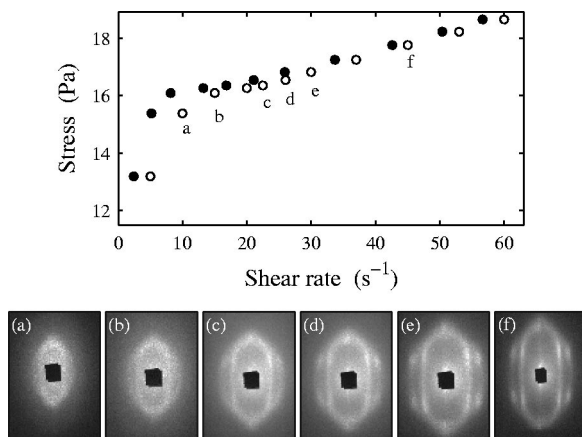

FIG. 6. ($\bigcirc$) Stationary flow curve obtained at $T = 30\,°C$ under controlled shear rate. The values (σ, $\dot{\gamma}$) are extracted from the temporal responses displayed in Fig. 5. ($\bullet$) True flow curve σ vs $\dot{\gamma}_{\text{true}}$. The true shear rates take into account the effect of wall slip and are calculated using Eq. (3) (see Sec. IV B). Corresponding diffraction patterns at $\dot{\gamma} = 10$ (a), 15 (b), 22.5 (c), 26 (d), 30 (e), and 45 s^{-1} (f). The increase of the ring diameter in (a)–(e) results from the decrease of the onion size. The field of the CCD camera has been adapted to the pattern size in the last diffraction pattern only, so that the apparent change of size is not physical in (f).
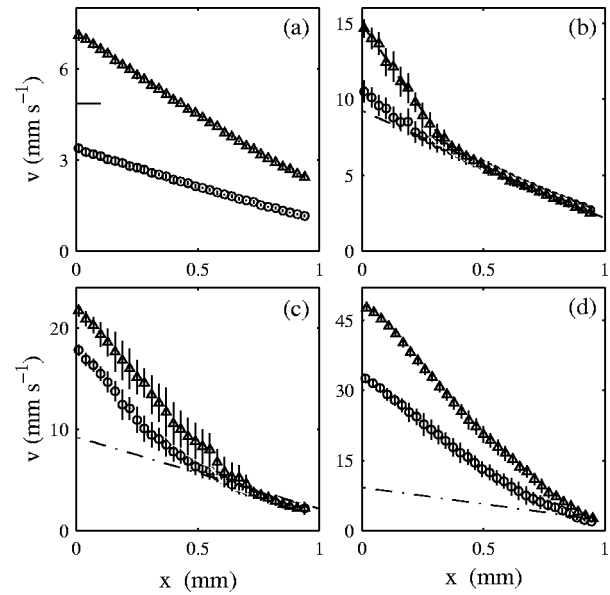

FIG. 7. Time-averaged velocity profiles obtained simultaneously to the flow curve displayed in Fig. 6. The error bars represent the temporal fluctuations of the local velocity (see text). (a) $\dot{\gamma} = 5$ ($\bigcirc$) and 10 s^{-1} ($\triangle$). The horizontal bar indicates the rotor velocity v_0 for $\dot{\gamma} = 5$ s^{-1} and helps to visualize wall slip at the rotor. (b) $\dot{\gamma} = 15$ ($\bigcirc$) and 20 s^{-1} ($\triangle$). The dashed line is a guide to the eye in the highly sheared band and corresponds to a local shear rate $\dot{\gamma}_B \approx 23$ s^{-1}. (c) $\dot{\gamma} = 22.5$ ($\bigcirc$) and 26 s^{-1} ($\triangle$). (d) $\dot{\gamma} = 37$ ($\bigcirc$) and 53 s^{-1} ($\triangle$). For (b)–(d), the dash-dotted line indicates the weakly sheared band and corresponds to a local shear rate $\dot{\gamma}_A \approx 7.1$ s^{-1}.

6(c)]. When the shear rate is further increased, peaks become more and more contrasted as can be seen in Figs. 6(d–f). The flow curve displays a change of slope around the layering transition but it is rather difficult to locate precisely the various regions of different structures from the rheological data alone and without the information inferred from the diffraction patterns. Significant shear thinning is observed: $\eta \approx 2.6$ Pa s at $\dot{\gamma} = 5$ s^{-1} and $\eta \approx 0.3$ Pa s at $\dot{\gamma} = 60$ s^{-1}.

Far below or far above the layering transition, well-defined profiles are easily measured. But very surprisingly, near the layering transition, the local velocity is not stationary but displays large temporal fluctuations while σ only fluctuates within a few percents (see Ref. [29] for a complete study). The characteristic times of these fluctuations range from 100 to 1000 s and are of the order of the time needed to obtain a full velocity profile (2–3 min). Such dynamics prevent us to record well-defined profiles. To obtain valuable data, we chose to measure *time-averaged* velocity profiles: several profiles were recorded at a given applied shear rate, and later averaged. The typical number of profiles needed to obtain good statistical estimates of the flow field ranges between 10 and 20. The standard deviations of those estimates yield the amplitudes of the temporal fluctuations. Figure 7 displays velocity profiles measured simultaneously to the flow curve of Fig. 6. Each profile corresponds to an average over up to 20 measurements. Error bars represent the standard deviations of the local velocities.

The main features of these profiles are as follows.

(i) Below the layering transition, i.e., for $\dot{\gamma} \lesssim \dot{\gamma}_1 \approx 15$ s^{-1}, velocity profiles are perfectly stationary; significant wall slip can be detected: the velocity at the stator does not vanish at $x=e$, and the fluid velocity does not reach the rotor velocity at $x=0$. Except very close to the walls where slippage occurs, the flow is homogeneous since the profiles are nearly linear.

(ii) At $\dot{\gamma} \gtrsim \dot{\gamma}_1$, a highly sheared band nucleates at the rotor. The local shear rate in this band is about $\dot{\gamma}_B \approx 23$ s^{-1} and the other band is locally sheared at $\dot{\gamma}_A \approx 7.1$ s^{-1} [see Fig. 7(b)]. Significant temporal fluctuations are present [29], and important wall slip can still be measured.

(iii) When the shear rate is further increased up to $\dot{\gamma} = \dot{\gamma}_2 \approx 37$ s^{-1}, the highly sheared band covers the whole gap. The value $\dot{\gamma}_A \approx 7.1$ s^{-1} of the weakly sheared band remains almost constant over the coexistence domain (15–37 s^{-1}).

(iv) For $\dot{\gamma} \gtrsim \dot{\gamma}_2$, the flow becomes homogeneous again. Temporal fluctuations of the velocity also disappear but the fluid still slips at the two walls.

Those results show without any ambiguity that the layering transition can be described by the classical phenomenology of shear banding. At $\dot{\gamma} \lesssim \dot{\gamma}_1$, the flow is homogeneous and corresponds to a disordered state of onions, as can be checked from the diffraction patterns. At $\dot{\gamma} \gtrsim \dot{\gamma}_1$, velocity profiles display two bands corresponding to two given local shear rates $\dot{\gamma}_A$ and $\dot{\gamma}_B$. At $\dot{\gamma} \gtrsim \dot{\gamma}_1$, peaks also appear on the ring. When the shear rate is further increased up to $\dot{\gamma}_2$, the width of the highly sheared band grows as well as the contrast of the peaks on the diffraction ring. At $\dot{\gamma} \gtrsim \dot{\gamma}_2$, the flow is homogeneous again and the contrast of the peaks on the ring is maximal.

Let us recall that the diffraction patterns correspond to a measure of the structure of the fluid *integrated* along the velocity gradient direction ∇v (see Fig. 1). Therefore, the contrast of the peaks on the ring provides an estimate of the relative proportion of layered vs disordered onions in the gap. Thus, the above results clearly point to a picture of the flow where the highly (weakly) sheared band corresponds to the layered (disordered) onions. The combined measurements of fluid structure, global rheology, and local velocity profiles presented above bring unambiguous evidence for banded flows associated with the layering transition in our lamellar phase. Similar results were reported by Callaghan and co-workers [24] in the case of a wormlike micellar system using nuclear magnetic resonance imaging, although the classical shear banding scenario (nucleation and growth of a highly sheared band) was not fully unveiled.

In the following paragraph, we present a detailed analysis of the slip velocities. We also demonstrate that the correction due to wall slip allows us to use a mechanical model to fit the velocity profiles consistently with the classical picture of shear banding.

B. Wall slip, true flow curve, and lubricating layers

1. True flow curve

Using the measured velocity profiles, it is easy to define a *true* shear rate in the bulk onion texture by $\dot{\gamma}_{\text{true}} = (v_1 - v_2)/e$, where v_1 (v_2, respectively) corresponds to the velocity of the fluid at $x=0$ ($x=e$, respectively) estimated from the measured velocity profiles. Moreover, in order to take into account the stress inhomogeneity in the Couette cell and thus get a quantitative comparison between this true shear rate and the engineering shear rate $\dot{\gamma}$ indicated by the rheometer, we define $\dot{\gamma}_{\text{true}}$ consistently with Eq. (2) by

$$\dot{\gamma}_{\text{true}} = \frac{R_1^2 + R_2^2}{R_1(R_1 + R_2)} \frac{v_1 - v_2}{e}. \tag{3}$$

Figure 6 presents the *true* flow curve $\sigma(\dot{\gamma}_{\text{true}})$ ($\bullet$) and the flow curve computed from the values indicated by the rheometer $\sigma(\dot{\gamma})$ ($\bigcirc$). The true shear rate allows us to remove the contribution due to wall slip. When compared to the engineering flow curve σ vs $\dot{\gamma}$, the true flow curve seems to reveal a stress plateau at a value of about 16 Pa. This plateau extends from $\dot{\gamma}_A \approx 7$ s^{-1} to $\dot{\gamma}_B \approx 25$ s^{-1}. Note that this stress plateau is not perfectly *flat* but presents a small slope. We will show in Sec. V that such a slope is due to the curvature of the Couette geometry as expected from theoretical models [44,45].

2. Lubricating layers

To explain the presence of wall slip in complex fluid flows, one usually considers that thin lubricating layers are present at the walls of the Couette cell. In emulsions, for instance, it is well established that wall slip is due to the presence of highly sheared thin films composed of the continuous phase only [46]. These films play the role of *lubricating layers*: the bulk material is weakly sheared, whereas the films *absorb* a part of the viscous stress. In our case, we can reasonably assume that wall slip is due to very thin layers composed of water or of a few membranes lying normally to the velocity gradient direction ∇v. The resolution of our setup (≈ 50 μm) does not allow us to measure *directly* the thicknesses of those layers.

However, in this simple picture, there is no discontinuity of the shear stress inside the gap of the Couette cell. Because the thicknesses of the lubricating layers are very small (≈ 100 nm), one can assume that the flow inside the films is laminar. Under this assumption, we may access the thicknesses of the lubricating layers. Indeed, let us define the slip velocity at the rotor $v_{s_1} = v_0 - v_1$ as the difference between the rotor velocity v_0 and the velocity v_1 at the rotor, and the slip velocity $v_{s_2} = v_2$ at the stator as the velocity v_2 measured at the stator. v_{si}/h_i then corresponds to the mean shear rate inside the film of thickness h_i ($i=1$ for the rotor and $i=2$ for the stator). By assuming that the stress is continuous inside the gap of the Couette cell, the thicknesses of the layers are then given by
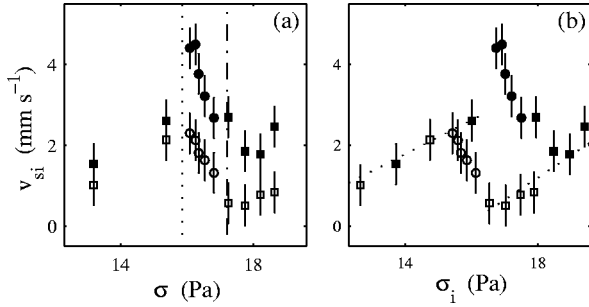
FIG. 8. (a) Sliding velocities v_{si} vs stress σ: v_{s1} at the rotor ($\blacksquare$,$\bullet$) and v_{s2} at the stator ($\square$,$\circ$). The dotted line indicates σ_A = 15.9 Pa and the dash-dotted line σ_B = 17.2 Pa (see text). (b) v_{si} vs local stress σ_i. The dotted lines are guidelines for the homogeneous states. ($\square$,$\blacksquare$) correspond to homogeneous velocity profiles and ($\circ$,$\bullet$) to banded velocity profiles.

$$h_i = \frac{\eta_f v_{s_i}}{\sigma_i}, \qquad (4)$$

where $\sigma_i = \sigma(R_i)$ is the *local* shear stress at wall number i and η_f is the viscosity of the lubricating layers. Note that in the Couette geometry the local stress is given by $\sigma(r) = \Gamma/(2\pi H r^2)$. Using Eq. (1), the local values σ_i at the walls are linked to the engineering stress σ indicated by the rheometer by

$$\sigma_i = \frac{2R_j^2}{R_1^2 + R_2^2}\sigma, \qquad (5)$$

where $j=2$ ($j=1$) when $i=1$ ($i=2$). Once again, it is important not to confuse the engineering value σ with the local values σ_1, σ_2, and more generally $\sigma(r)$.

3. Wall slip and shear banding

Figure 8(a) presents the slip velocities v_{si} vs the engineering stress σ, both at the stator ($\square$,$\circ$) and at the rotor ($\blacksquare$,$\bullet$). The homogeneous profiles are indicated by squares ($\square$,$\blacksquare$) and banded flows by circles ($\circ$,$\bullet$). Figure 8(a) reveals the three regimes previously observed on both velocity profiles and diffraction patterns.

(i) when $\sigma < \sigma_A \approx 15.9$ Pa, the velocity profiles are nearly linear and the flow is only composed of disordered onions. In this region, the slip velocities v_{si} slightly increase under increasing stress σ.

(ii) When $\sigma_A \lesssim \sigma \lesssim \sigma_B \approx 17.2$ Pa, the nucleation and growth of the highly sheared band corresponding to the layered state is associated with a decrease of v_{si} with σ.

(iii) When $\sigma > \sigma_B$, the flow is homogeneous again and the slip velocities v_{si} slightly increase with σ. Note that the exact values of σ_A and σ_B indicating the coexistence domain will be calculated using Eqs. (15) and (16) in Sec. V.

Figure 8(b) presents the same slip velocities but plotted against the local stress σ_i inferred from Eq. (5). It reveals two important results.

(i) When the flow is homogeneous, the slip velocities at the rotor v_{s1} and at the stator v_{s2} collapse on the same curve
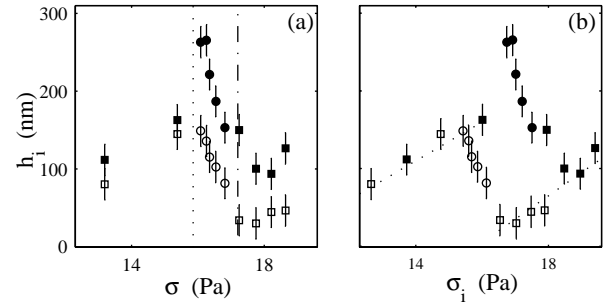

FIG. 9. (a) Thicknesses h_i of the sliding layer vs stress σ: h_1 at the rotor ($\blacksquare$,$\bullet$) and h_2 at the stator ($\square$,$\circ$). The dotted line indicates σ_A = 15.9 Pa and the dash-dotted line σ_B = 17.2 Pa (see text). (b) h_i vs local stress σ_i. The dotted lines are guidelines for the homogeneous states. ($\square$,$\blacksquare$) correspond to homogeneous velocity profiles and ($\circ$,$\bullet$) to banded velocity profiles.

when plotted against the local stresses σ_1 and σ_2. In other words, v_{si} seem to be a unique function of the local stress in the homogeneous domains, i.e., $v_{si} = f(\sigma_i)$. This feature is also observed in concentrated colloidal systems where inertial effects are totally suppressed by the osmotic pressure needed to concentrate the colloids [46,47].

(ii) In the coexistence domain, i.e., for $\sigma_A \lesssim \sigma \lesssim \sigma_B$, there is a large difference between slip velocities at the rotor and at the stator, even when v_{si} are plotted against the local stress σ_i. This result confirms the observed structuration: wall slip is very different at the two walls because there are *two* different fluids inside the gap (the layered state of onions lies near the rotor whereas the disordered onions lie near the stator). In the coexistence domain, the fact that the slip velocity v_{si} is a unique function of the local stress σ_i does not hold anymore. Moreover, our data clearly indicate that wall slip is larger at the rotor than at the stator in this domain.

4. Thicknesses of the lubricating layers

Figure 9 presents the thicknesses h_i of the lubricating layers calculated from Eq. (4) and assuming that the viscosity of the lubricating films is $\eta_f = 10^{-3}$ Pa s, the viscosity of water. The thicknesses h_i are of the order of 100–200 nm. Such a value is in good agreement with other measurements performed in concentrated colloidal systems [46,47]. Let us recall that in the case of our lamellar phase, the smectic period d is 15 nm, so that it is reasonable to assume that the lubricating layers are composed of only water or a few membranes (≈ 10), perfectly aligned along the walls. In any case, the viscosity of the film is probably of the order of 10^{-3} Pa s.

5. A possible explanation for the origin of lubricating layers and their variations with σ

In the onion texture, flow can *compress* the onions by changing the smectic period d. Such a compression expels some water from inside the onions and helps to lubricate the flow. This effect has been shown in a lot of lyotropic lamellar phases using neutron and x-ray diffraction [26,48]. In our system, as measured with neutron scattering, the smectic pe-
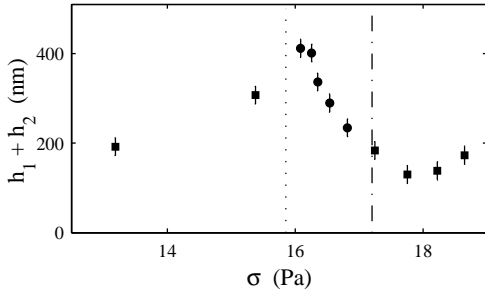
FIG. 10. $h_1 + h_2$ vs stress σ. The dotted line indicates $\sigma_A = 15.9$ Pa and the dash-dotted line $\sigma_B = 17.2$ Pa (see text). (■) corresponds to homogeneous velocity profiles and (●) to banded velocity profiles.

riod changes slightly over the range of $\dot{\gamma}$ under study [26]. If we assume that the expelled water can also *migrate* from the bulk material to the walls in order to lubricate the flow, the quantity $h_1 + h_2$ is then proportional to the volume of water in the lubricating layers. Figure 10 presents $h_1 + h_2$ vs σ. Again, the three regions of the shear banding phenomenology can be clearly identified from Fig. 10. At low applied stress, the quantity of water at the walls increases under increasing stress. This confirms the assumption that the viscous stress compresses the onions and expels some water. At intermediate stress, in the coexistence domain, the volume of water decreases while the width of the highly sheared band grows in the gap of the Couette cell.

Such a result may be simply explained if one considers that some water is needed to lubricate the flow between the layers of ordered onions. Indeed, as suggested in Ref. [26], the layering of onions is probably associated with the expulsion of some water from the onions to lubricate the flow between the layers. The decrease of $h_1 + h_2$ could be the signature of a *migration* of the water from the walls to the bulk of the highly sheared band. At higher stress, when the layered band has invaded the gap, $h_1 + h_2$ increases again with the shear stress σ. This is consistent with the fact that the viscous stress tends to compress the onions in the homogeneous layered state. Such a picture, suggested by our experiments and by previous works [26], is obviously highly hypothetical. Resolved x-ray or neutron scattering techniques performed in the gap of the Couette cell are needed to confirm such assumptions.

V. A SIMPLE MECHANICAL APPROACH OF THE SHEAR-BANDING INSTABILITY

A. Local constitutive flow curve

The aim of this section is to determine whether the classical mechanical picture of the shear banding instability holds in our experiments. In such a picture, the flow curve is the one sketched in Fig. 11. Two branches, corresponding to the two different organizations of onions, are separated by a coexistence domain. The rheological behaviors of the two branches are given by $\sigma = f_i(\dot{\gamma})$, where $i = 1$ ($i = 2$) stands for the disordered (layered) state of onions. In the simple picture of shear banding, one generally assumes that the flow
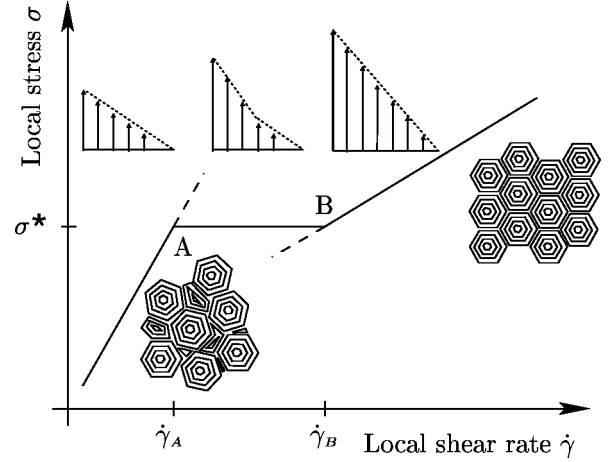

FIG. 11. Local constitutive flow curve of the layering transition. Two branches corresponding to the two different structures of onions are separated by a stress plateau at σ^*. The interface between bands of different local shear rates $\dot{\gamma}_A$ and $\dot{\gamma}_B$ is stable at a unique stress σ^*. The highly sheared band nucleates at point A and invades the gap up to point B where the flow becomes homogeneous again.

field can separate between bands of different structures, whose local rheological behaviors are given by $\sigma = f_i(\dot{\gamma})$. One also assumes that the interfaces between the bands are only stable at a critical stress σ^*. When the shear rate is imposed in a geometry where stress is homogeneous (e.g., a cone-and-plate geometry), such an assumption leads to a *stress plateau* on the flow curve at σ^* [44]. On the plateau, velocity profiles display bands of local shear rates $\dot{\gamma}_A$ and $\dot{\gamma}_B$. The following equation relates the imposed *global* shear rate to the proportion of bands *locally* sheared at $\dot{\gamma}_A$ and $\dot{\gamma}_B$:

$$\dot{\gamma} = \alpha \dot{\gamma}_A + (1 - \alpha) \dot{\gamma}_B, \qquad (6)$$

where α is the volume fraction of bands locally sheared at $\dot{\gamma}_A$. In stress-controlled experiments, the plateau cannot be seen anymore and one observes a discontinuous jump between $\dot{\gamma}_A$ and $\dot{\gamma}_B$ when the stress is slightly increased above σ^*. In the following paragraph, we addresss the validity of the assumption that interfaces lie at a critical stress σ^*.

B. Width of the highly sheared band in the Couette geometry

In the Couette geometry, the stress is not homogeneous inside the gap of the cell and the simple analysis presented above does not hold anymore. Indeed, the local stress $\sigma(r)$, where r is the radial position in the flow, is given by

$$\sigma(r) = \frac{\Gamma}{2\pi H r^2} = \sigma_1 \frac{R_1^2}{r^2}, \qquad (7)$$

where Γ is the imposed torque and $\sigma_1 = \Gamma/(2\pi H R_1^2)$ is the stress at the rotor. The shear-banding scenario then leads to a picture with only two bands: one locally sheared at $\dot{\gamma}_A$ and one locally sheared at $\dot{\gamma}_B$. If one considers that the interface
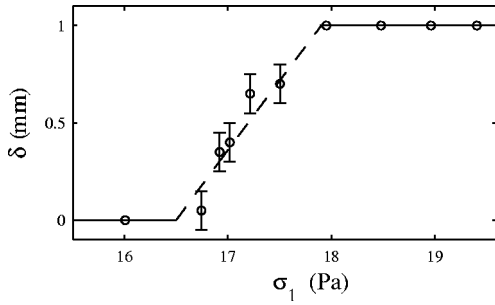
FIG. 12. Width δ of the highly sheared band vs σ_1 the stress at the rotor. The dashed line corresponds to Eq. (8) with $\sigma^* = 16.5$ Pa.

between bands is only stable at a given stress σ^*, one easily calculates the width δ of the highly sheared band:

$$\delta = R_1 \left(\sqrt{\frac{\sigma_1}{\sigma^*}} - 1 \right). \qquad (8)$$

Such a relation shows that the stress should increase slightly along the coexistence domain. Indeed, when entering the co-existence region, i.e., when $\delta = 0$, one finds $\sigma_1 = \sigma^*$, and when the highly sheared band has invaded the gap, $\delta = e$ and $\sigma_1 = (R_2/R_1)^2 \sigma^*$. This means that, in the Couette geometry, the plateau is not perfectly flat and presents a slope $(R_2/R_1)^2 - 1 \approx 2e/R_1$ due to the stress inhomogeneity [44]. Note that if the concentrations of the two structures differ, one also expects a nonflat plateau. In our system, the only stress inhomogeneity seems to account well for the slope of the plateau. Therefore, concentration effects are not included here.

Our velocimetry measurements easily yield the width δ of the highly sheared band. Figure 12 displays the measured δ vs the measured stationary stress at the rotor σ_1. We have also added in this figure the theoretical relation of Eq. (8) with $\sigma^* = 16.5$ Pa, which yields a satisfactory agreement with the experimental data. This seems to indicate that the stability criterion for the interface holds in our experiments with $\sigma^* = 16.5$ Pa. However, our data present relatively large error bars on the measured δ. To proceed further in the analysis and to confirm the mechanical picture of the shear banding instability, one should now try to fit all the measured velocity profiles from the knowledge of the flow curve.

C. Procedure for fitting the velocity profiles

Our fitting procedure relies on the following relations:

$$\sigma(r) = \frac{\Gamma}{2\pi H r^2}, \qquad (9)$$

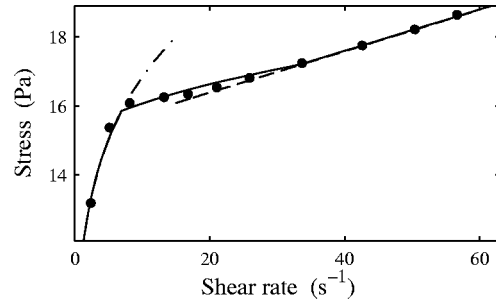$$\dot{\gamma}(r) = r \frac{\partial}{\partial r} \left(\frac{v}{r} \right). \qquad (10)$$

FIG. 13. ($\bullet$) True flow curve σ vs $\dot{\gamma}_{\text{true}}$ displayed in Fig. 6. The dash-dotted line is the best fit of the low sheared branch ($\dot{\gamma} \leq 6$ s^{-1}) using a shear-thinning behavior $\sigma = A\dot{\gamma}^n$ with $A = 11.49$ and $n = 0.17$. The dashed line is the best fit of the highly sheared branch ($\dot{\gamma} \geq 30$ s^{-1}) according to a Bingham behavior $\sigma = \sigma_0 + \eta\dot{\gamma}$ with $\sigma_0 = 15.19$ Pa and $\eta = 0.06$ Pa s. The continuous line is computed from Eqs. (11)–(14) with $\sigma^* = 16.5$ Pa.

In order to compute velocity profiles from Eqs. (9) and (10), we first have to determine the rheological laws linking the local stress $\sigma(r)$ and the local shear rate $\dot{\gamma}(r)$.

1. Rheological behaviors of the homogeneous branches

Figure 13 presents the true flow curve $\sigma(\dot{\gamma}_{\text{true}})$ measured in our experiment at $T = 30\,°\text{C}$ and under controlled shear rate. We have fitted the two branches corresponding to the two homogeneous states: (i) for $\dot{\gamma} \leq 6$ s^{-1} (disordered on-ions) by a shear-thinning behavior $\sigma = f_1(\dot{\gamma}) = A\dot{\gamma}^n$ with $A = 11.49$ and $n = 0.17$ and (ii) for $\dot{\gamma} \geq 30$ s^{-1} (layered state) by a Bingham fluid $\sigma = f_2(\dot{\gamma}) = \sigma_0 + \eta\dot{\gamma}$ with $\sigma_0 = 15.19$ Pa and $\eta = 0.06$ Pa s. The resulting fits are presented in Fig. 13. Since the flow field is homogeneous on these branches, such behaviors fitted from the true flow curve, i.e., after contributions due to wall slip are removed, represent the local rheological behavior σ vs $\dot{\gamma}$.

2. Equations for the theoretical flow curve and the velocity profiles

Let us now assume that the interface between the bands lies at a unique stress σ^* and let us consider a given torque Γ. From Γ and Eq. (9), we get the local stress $\sigma(r)$. If $\sigma(r) < \sigma^*$ everywhere in the gap of the Couette cell, the flow is homogeneous and composed of the disordered on-ions, whereas if $\sigma(r) > \sigma^*$ everywhere, the flow is also ho-mogeneous but composed of the layered state of onions. Moreover, the local shear rate $\dot{\gamma}(r)$ is given by Eq. (10), so that in both cases, the velocity profiles are given by the fol-lowing integration of the rheological behaviors:

$$\frac{v(r)}{r} = \frac{v_2}{R_2} + \int_{R_2}^r \frac{\dot{\gamma}(u)}{u} du, \qquad (11)$$

where $\dot{\gamma}(r)$ is found by solving

$$\sigma(r) = \frac{\Gamma}{2\pi H r^2} = f_i(\dot{\gamma}(r)), \tag{12}$$

and i denotes the considered branch.

When there exists one particular position in the gap where $\sigma(r) = \sigma^*$, the flow is inhomogeneous and composed of two different bands. To calculate the resulting velocity profile, one should separate the previous integration according to

$$\frac{v(r)}{r} = \frac{v_2}{R_2} + \int_{R_2}^{r} \frac{\dot{\gamma}(u)}{u} du \quad \text{for } r > R_1 + \delta$$

and

$$\frac{v(r)}{r} = \frac{v(R_1 + \delta)}{R_1 + \delta} + \int_{R_1 + \delta}^{r} \frac{\dot{\gamma}(u)}{u} du \quad \text{for } r < R_1 + \delta, \tag{13}$$

where δ is given by Eq. (8), and $\dot{\gamma}(r)$ by

$$\sigma(r) = f_1(\dot{\gamma}(r)) \quad \text{for } r > R_1 + \delta,$$

$$\sigma(r) = f_2(\dot{\gamma}(r)) \quad \text{for } r < R_1 + \delta. \tag{14}$$

The Appendix presents the detailed integration of Eqs. (11)–(14) for the specific behaviors $\sigma = f_1(\dot{\gamma})$ and $\sigma = f_2(\dot{\gamma})$ obtained previously. Note that Eqs. (11)–(14) require the knowledge of $v_{s2} = v_2$ for the arbitrary torque Γ. Thus, to compute v_{s2} at any value of Γ, we first interpolate the data v_{si} vs σ displayed in Fig. 8(a).

For each value of Γ, i.e., for each value of σ indicated by the rheometer [see Eq. (1)], one can calculate a theoretical velocity profile $v(x)$ using the fitting procedure detailed above. One can then calculate the corresponding true shear rate $\dot{\gamma}_{\text{true}}$ using Eq. (3). Such a procedure allows us to compute a theoretical flow curve σ vs $\dot{\gamma}_{\text{true}}$. This theoretical flow curve is displayed in Fig. 13 for comparison with the measured rheological data. The coexistence domain is well reproduced by this theoretical true flow curve, namely, the slope of the stress plateau. This good agreement confirms the assumption that the interface between the bands lies at a given value of the stress σ^*. Note that the value $\sigma^* = 16.5$ Pa is the only free parameter of the fitting procedure. The value of σ^* also yields the value of the stress σ_A (σ_B) at the entrance (at the end) of the coexistence domain:

$$\sigma_A = \frac{R_1^2 + R_2^2}{2R_2^2} \sigma^* \approx 15.9 \text{ Pa}, \tag{15}$$

$$\sigma_B = \frac{R_1^2 + R_2^2}{2R_1^2} \sigma^* \approx 17.2 \text{ Pa}. \tag{16}$$

The above values of σ_A and σ_B are those displayed in Figs. 8–10 to visualize the coexistence domain.

For each value of Γ and thus for each theoretical velocity profile, one can also calculate the shear rate $\dot{\gamma}$ indicated by
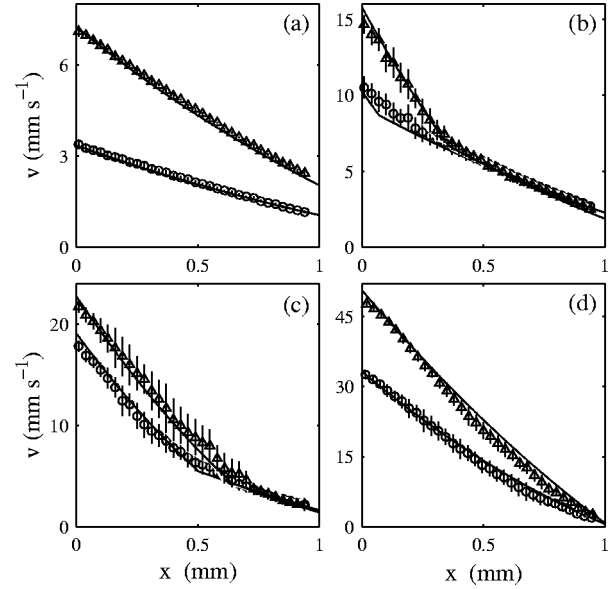

FIG. 14. Time-averaged velocity profiles displayed in Fig. 7. $\dot{\gamma} = 5$ (○) and 10 s^{-1} (△). (b) $\dot{\gamma} = 15$ (○) and 20 s^{-1} (△). (c) $\dot{\gamma} = 22.5$ (○) and 26 s^{-1} (△). (d) $\dot{\gamma} = 37$ (○) and 53 s^{-1} (△). The error bars represent the temporal fluctuations of the local velocity. The continuous lines are the theoretical velocity profiles calculated from Eqs. (11)–(14).

the rheometer. Indeed, it is easy to determine the rotor velocity from $v(x)$ and from the values of v_{s1} displayed in Fig. 8(b): $v_0 = v(x=0) + v_{s1}$. $\dot{\gamma}$ is then given by Eq. (2). From the calculated velocity profiles, we extracted those corresponding to the shear rates applied in our experiments. Figure 14 shows these theoretical fits $v(x)$ and the corresponding experimental velocity profiles. Again, the good agreement indicates that the stability criterion for the interface holds in our experiments. Such an agreement also confirms the observed shear banding phenomenology and more precisely, the fact that near the layering transition, the flow is composed of two different bands characterized by two different rheological behaviors.

D. Discussion on the validity of the mechanical approach

In the previous mechanical approach, it is important to note that to each value of torque Γ and thus to each value of stress σ, we can associate a unique velocity profile $v(x)$, and thus a unique shear rate $\dot{\gamma}$. This is a direct consequence of the slope of the stress plateau of the flow curve in the Couette geometry. The uniqueness of $\dot{\gamma}$ for a given σ means that the shear banding phenomenology is also expected when the stress is controlled in a Couette geometry. However, as mentioned in Sec. II B (see Fig. 2), the responses of the shear rate under controlled stress for temperatures $T \geq T_c = 27\,°C$ are no longer stationary and present large oscillations in the vicinity of the layering transition. It is thus obvious that some ingredients are missing in the mechanical approach detailed previously to model such dynamics. For temperatures $T < T_c$, the responses of the shear rate under controlled
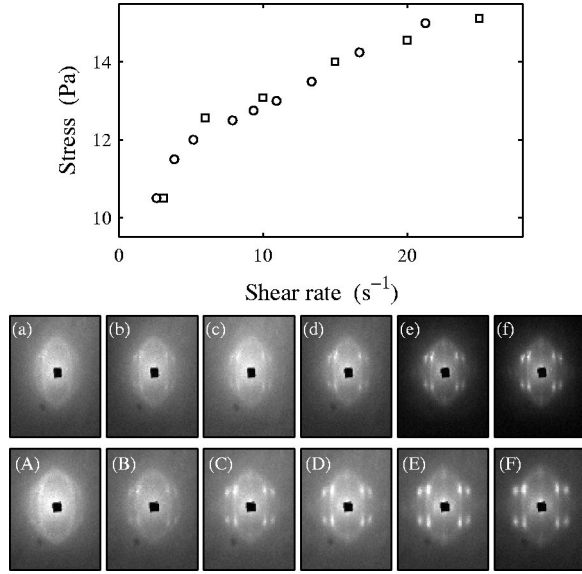
FIG. 15. Stationary flow curves obtained at $T=26\,°C$ under controlled stress ($\bigcirc$) and under controlled shear rate ($\square$). Corresponding diffraction patterns at imposed stress: (a) $\sigma=12$, (b) 12.5, (c) 12.75, (d) 13, (e) 13.5, and (f) 14.25 Pa. Corresponding diffraction patterns at imposed shear rate: (A) $\dot{\gamma}=6$, (B) 10, (C) 15, (D) 20, (E) 25, and (F) 30 s^{-1}.

stress are almost stationary and only display relatively small fluctuations at the layering transition. Our mechanical approach may thus be fully validated only at $T<T_c$. This led us to repeat our experiments at $T=26\,°C$ both under controlled stress and under controlled shear rate.

Using careful protocols similar to that of Sec. IV A, we measure the two stationary flow curves displayed in Fig. 15, as well as the corresponding diffraction patterns. Figure 16 presents the time-averaged velocity profiles measured simultaneously to the flow curves displayed in Fig. 15. These experiments clearly demonstrate that the phenomenology of shear banding, previously observed at $T=30\,°C$ under controlled $\dot{\gamma}$, is also recovered at $T=26\,°C$ both at imposed $\dot{\gamma}$ and imposed σ. As expected from the mechanical approach, there is no difference between controlling the stress or the

shear rate in the Couette geometry, as long as the rheological responses are stationary.

VI. CONCLUSIONS

In this paper, we have presented an extensive study of a shear-induced transition in a lyotropic system: the layering transition of the onion texture. Using velocimetry, structural measurements and rheological data, we have shown that the classical picture of shear banding holds for the layering transition. In this picture, velocity profiles display bands in the vicinity of the transition and the nucleation and growth of the highly sheared band is associated with the nucleation and growth of the SIS, i.e., of the layered state of onions. Using the classical mechanical approach [12,15], in which the interface between the bands lies at a given value of the stress, we were able to fit the velocity profiles and the coexistence domain on the flow curve.

Moreover, our data reveal the presence of strong wall slip. We have shown that the variations of wall slip with stress are in good agreement with the shear banding behavior: when the flow is homogeneous, the slip velocity is a universal function of σ since inertial effects are negligible, and when the flow displays bands, wall slip presents a very large dissymmetry at the rotor and at the stator, probably because the two different textures have different behaviors at the walls of the Couette cell.

One of the most puzzling features of our results is the presence of large temporal fluctuations of the flow field in the coexistence domain. Indeed, velocity profiles display localized temporal fluctuations reaching up to 20% at the interface between the two bands. Moreover, the characteristic times of such fluctuations are very long (100–1000 s), and do not correspond to external mechanical vibrations of the Couette cell. In the next part of the paper [29], we analyze in detail these temporal fluctuations.

APPENDIX

In the particular case of the rheological behaviors obtained in Sec. V C 1, i.e., the disordered texture $\sigma=f_1(\dot{\gamma})$ has a shear-thinning behavior $\sigma=A\dot{\gamma}^n$ and the layered state $\sigma=f_2(\dot{\gamma})$ is a Bingham fluid $\sigma=\sigma_0+\eta\dot{\gamma}$, Eqs. (11)–(14) read as follows.
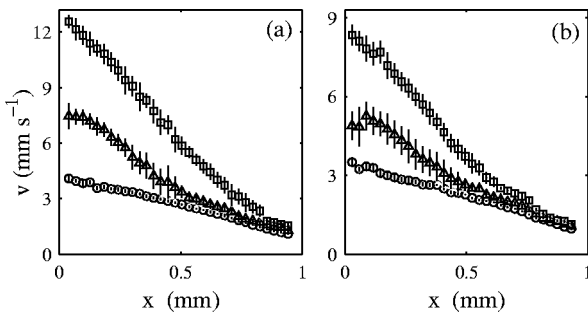
(i) If $\sigma(r)<\sigma^*$, the velocity profile is given by

FIG. 16. Time-averaged velocity profiles measured simultaneously to the flow curves displayed in Fig. 15 at $T=26\,°C$. The error bars represent the temporal fluctuations of the local velocity. (a) Imposed shear rate: $\dot{\gamma}=6$ ($\bigcirc$), 10 ($\triangle$), and 15 s^{-1} ($\square$). (b) Imposed stress: $\sigma=12$ ($\bigcirc$), 12.5 ($\triangle$), and 13 Pa ($\square$).

$$v(x)=v_{s2}\frac{r}{R_2}+r\frac{n}{2}\left[\frac{\Gamma}{2\pi HR_2^2 A}\right]^{1/n}\left[\left(\frac{R_2}{r}\right)^{2/n}-1\right].$$

(ii) If $\sigma(r) > \sigma^*$, the flow is also homogeneous and the velocity profile reads,

$$v(x) = v_{s2}\frac{r}{R_2} + r\frac{\Gamma}{4\pi H R_2^2 \eta}\left[\left(\frac{R_2}{r}\right)^2 - 1\right] + r\frac{\sigma_0}{\eta}\ln\left(\frac{r}{R_2}\right).$$

(iii) If there exists r for which $\sigma(r) = \sigma^*$, the flow displays two bands, and for $R_1 + \delta < r < R_2$,

$$v(x) = v_{s2}\frac{r}{R_2} + r\frac{n}{2}\left[\frac{\Gamma}{2\pi H R_2^2 A}\right]^{1/n}\left[\left(\frac{R_2}{r}\right)^{2/n} - 1\right],$$

whereas for $R_1 < r < R_1 + \delta$,

$$v(x) = r\frac{\Gamma}{4\pi H (R_1 + \delta)^2 \eta}\left[\left(\frac{R_1 + \delta}{r}\right)^2 - 1\right] + r\frac{\sigma_0}{\eta}\ln\left(\frac{r}{R_1 + \delta}\right)$$

$$+ v_{s2}\frac{r}{R_2} + r\frac{n}{2}\left[\frac{\Gamma}{2\pi H R_2^2 A}\right]^{1/n}\left[\left(\frac{R_2}{R_1 + \delta}\right)^{2/n} - 1\right].$$

[1] R.G. Larson, *The Structure and Rheology of Complex Fluids* (Oxford University Press, Oxford, 1999).

[2] E. Guyon, J.-P. Hulin, and L. Petit, *Hydrodynamique Physique* (InterÉditions/Éditions du CNRS, Paris, 1994).

[3] *Soft and Fragile Matter: Non Equilibrium Dynamics Metastability and Flow,* edited by M.E. Cates and M.R. Evans (Institute of Physics, Bristol, 2000).

[4] P. Hébraud, F. Lequeux, J.P. Munch, and D.J. Pine, Phys. Rev. Lett. **78**, 4657 (1997).

[5] J.-F. Berret, D.C. Roux, and G. Porte, J. Phys. II **4**, 1261 (1994).

[6] V. Schmitt, F. Lequeux, A. Pousse, and D. Roux, Langmuir **10**, 955 (1994).

[7] O. Diat, D. Roux, and F. Nallet, J. Phys. II **3**, 1427 (1993).

[8] D. Roux, F. Nallet, and O. Diat, Europhys. Lett. **24**, 53 (1993).

[9] Y.T. Hu, P. Boltenhagen, and D.J. Pine, J. Rheol. **42**, 1185 (1998).

[10] E. Eiser, F. Molino, G. Porte, and O. Diat, Phys. Rev. E **61**, 6759 (2000).

[11] L. Ramos, F. Molino, and G. Porte, Langmuir **16**, 5846 (2000).

[12] N.A. Spenley, M.E. Cates, and T.C.B. McLeish, Phys. Rev. Lett. **71**, 939 (1993).

[13] A. Kabla and G. Debrégeas, Phys. Rev. Lett. **90**, 258303 (2003).

[14] P.D. Olmsted and P.M. Goldbart, Phys. Rev. A **46**, 4966 (1992).

[15] C.-Y.D. Lu, P.D. Olmsted, and R.C. Ball, Phys. Rev. Lett. **84**, 642 (2000).

[16] J.L. Goveas and P.D. Olmsted, Eur. Phys. J. E **6**, 79 (2001).

[17] X.-F. Yuan, Europhys. Lett. **46**, 542 (1999).

[18] A. Ajdari, Phys. Rev. E **58**, 6294 (1998).

[19] G. Picard, A. Ajdari, L. Bocquet, and F. Lequeux, Phys. Rev. E **66**, 051501 (2002).

[20] E. Cappelaere, J.-F. Berret, J.-P. Decruppe, R. Cressely, and P. Lindner, Phys. Rev. E **56**, 1869 (1997).

[21] S. Lerouge, J.-P. Decruppe, and C. Humbert, Phys. Rev. Lett. **81**, 5457 (1998).

[22] R.W. Mair and P.T. Callaghan, Europhys. Lett. **36**, 719 (1996).

[23] M.M. Britton and P.T. Callaghan, Eur. Phys. J. B **7**, 237 (1999).

[24] E. Fischer and P.T. Callaghan, Phys. Rev. E **64**, 011501 (2001).

[25] J.-B. Salmon, A. Colin, S. Manneville, and F. Molino, Phys. Rev. Lett. **90**, 228303 (2003).

[26] O. Diat, D. Roux, and F. Nallet, Phys. Rev. E **51**, 3296 (1995).

[27] P. Sierro and D. Roux, Phys. Rev. Lett. **78**, 1496 (1997).

[28] J.-B. Salmon, S. Manneville, A. Colin, and B. Pouligny, Eur. Phys. J.: Appl. Phys. **22**, 143 (2003).

[29] J.-B. Salmon, S. Manneville, and A. Colin, Phys. Rev. E **68**, 051504 (2003).

[30] G. Porte, J. Appell, P. Bassereau, J. Marignan, M. Skouri, I. Billard, and M. Delsanti, Physica A **176**, 168 (1991).

[31] D. Roux, C. Coulon, and M.E. Cates, J. Phys. Chem. **96**, 4174 (1992).

[32] P. Hervé, D. Roux, A.-M. Bellocq, F. Nallet, and T. Gulik-Krzywicki, J. Phys. II **3**, 1255 (1993).

[33] W. Helfrich, Z. Naturforsch. A **33a**, 305 (1978).

[34] B.J. Ackerson and P.N. Pusey, Phys. Rev. Lett. **61**, 1033 (1988).

[35] A.-S. Wunenburger, A. Colin, J. Leng, A. Arnéodo, and D. Roux, Phys. Rev. Lett. **86**, 1374 (2001).

[36] J.-B. Salmon, A. Colin, and D. Roux, Phys. Rev. E **66**, 031505 (2002).

[37] M. Grosso, R. Keunings, S. Crescitelli, and P.L. Maffettone, Phys. Rev. Lett. **86**, 3184 (2001).

[38] M.E. Cates, D.A. Head, and A. Ajdari, Phys. Rev. E **66**, 025202 (2002).

[39] B.J. Berne and R. Pecora, *Dynamic Light Scattering* (Wiley, New York, 1995).

[40] B.J. Ackerson and N.A. Clark, J. Phys. **42**, 929 (1981).

[41] G.G. Fuller, J.M. Rallison, R.L. Schmidt, and L.G. Leal, J. Fluid Mech. **100**, 555 (1980).

[42] K.J. Måløy, W. Goldburg, and H.K. Pak, Phys. Rev. A **46**, 3288 (1992).

[43] J.P. Gollub and M.H. Freilich, Phys. Rev. Lett. **33**, 1465 (1974).

[44] O. Radulescu and P.D. Olmsted, J. Non-Newtonian Fluid Mech. **91**, 143 (2000).

[45] S.M. Fielding and P.D. Olmsted, Eur. Phys. J. E **11**, 65 (2003).

[46] H.A. Barnes, J. Non-Newtonian Fluid Mech. **56**, 221 (1995).

[47] J.-B. Salmon, L. Bécu, S. Manneville, and A. Colin, Eur. Phys. J. E **10**, 209 (2003).

[48] S.E. Welch, M.R. Stetzer, G. Hu, E.B. Sirota, and S.H.J. Idziak, Phys. Rev. E **65**, 061511 (2002).